Manipulation of Dirac Fermions in Nanochain-Structured Graphene

Wen-Han Dong(董文翰)[1†], De-Liang Bao(包德亮)[1†], Jia-Tao Sun(孙家涛)[2*],
Feng Liu(刘峰)[3], and Shixuan Du(杜世萱)[1,4,5*]

[1]*Institute of Physics and University of Chinese Academy of Sciences, Chinese Academy of Sciences,
Beijing 100190, China*
[2]*School of Information and Electronics, MIIT Key Laboratory for Low-Dimensional Quantum Structure and Devices,
Beijing Institute of Technology, Beijing 100081, China*
[3]*Department of Materials Science and Engineering, University of Utah, Salt Lake City, Utah 84112, USA*
[4]*CAS Center for Excellence in Topological Quantum Computation, Beijing 100190, China*
[5]*Songshan Lake Materials Laboratory, Dongguan 523808, China*

Graphene has afforded an ideal 2D platform for investigating a rich and fascinating behavior of Dirac fermions. Here, we develop a theoretical mechanism for manipulating the Dirac fermions in graphene, such as from type-I to type-II and type-III, by a top-down nanopatterning approach. We demonstrate that by selective chemical adsorption to pattern the 2D graphene into coupled 1D armchair chains (ACs), the intrinsic isotropic upright Dirac cone becomes anisotropic and strongly tilted. Based on model analyses and first-principles calculations, we show that both the shape and tilt of Dirac cone can be tuned by the species of chemisorption, e.g., halogen vs hydrogen, which modifies the strength of inter-AC coupling. Furthermore, the topological edge states and transport properties of the engineered Dirac fermions are investigated. Our work sheds lights on understanding the Dirac fermions in a nanopatterned graphene platform, and provides guidance for designing nanostructures with novel functionality.

The discovery of graphene[1,2] ushered a blossoming of topological materials hosting quasiparticle-like fermions and bosons.[3−9] Especially, Dirac fermions in graphene exhibit a rich spectra of phenomena, such as quantum Hall effect,[10,11] Klein tunneling[12] and quantum transport,[13,14] which have also been extended to artificial acoustic[15] and photonic[16] Dirac systems. Recent discovery of type-II and type-III Dirac fermions in topological semimetals[17−19] further enriches the Dirac physics with novel Fermi surface and band topology, as manifested in gapless plasmon mode[20] and nodeless superconductivity.[21] The varying types of Dirac states[22,23] mean different transport properties[24] and magnetic response,[25] offering new opportunity for quantum and spintronics device applications.

Beyond graphene, several two-dimensional (2D) carbon- and boron-based nanostructures[26−28] have been predicted with Dirac fermions. Different types of Dirac Fermions have also been predicted in a few carbon allotropes with bipartite-symmetry breaking penta-rings.[29,30] However, each individual material hosts inherently one particular type of Dirac Fermions. It will be fundamentally interesting and

practically useful to develop a scheme to manipulate Dirac Fermions into different types in one single material platform, to realize different device functionalities.

Traditionally there are two distinct approaches towards nanofabrication of quantum materials: the bottom-up[31] or top-down approach.[32,33] Similarly, such approaches can be adopted in creating novel nanostructured topological materials. As an example of the bottom-up approach, recent studies have shown three-dimensional (3D) "nanowire-structured" bulk materials assembled from 1D bismuth-halides (Bi_4Br_4 and Bi_4I_4) chains, to display tunable topological phases of weak topological insulator (TI) and high order TI.[34−36] As an example of top-down approach, the van der Waals (vdW) layered 2H-NbTe$_2$ has been modulated into one-dimensional (1D) stripe-like patterns by silicon intercalation, to induce formation of directional Dirac fermions.[37,38] Researchers also observed the emergence of multiple Dirac cones in high mobility graphene devices with a gate-tunable 1D superlattice.[39] Moreover, the atomic-thick BeN$_4$ layers consisting of polyacetylene-like nitrogen chains were reported to host anisotropic Dirac fermions.[40] These progresses offer new insights into Dirac fermions

based on nanochain-structured materials, i.e., nanostructures with distinct 1D building blocks or 1D electronic patterns. Noting that 2D graphene consists of basic building blocks of 1D armchair and zigzag chains, it is desirable to create nanochain-structured graphene, to tune the properties of Dirac fermions.

In this Letter, we demonstrate theoretically a top-down approach towards constructing nanochain-structured graphene and manipulating the tilting degree and anisotropy of Dirac fermions. By selective chemisorption, 2D graphene is nanopatterned into coupled 1D armchair chains (ACs), which by themselves *in isolation* represent the 1D Su–Schrieffer–Heeger (SSH) model.[41,42] Using $k \cdot p$ analysis and a tight-binding model, we show that *collectively* the coupled ACs can host strongly tilted Dirac cones depending on the strength of interchain coupling. Using first-principles calculations, we confirm the transition of Dirac fermions from type-I to type-II and type-III, by tuning the interchain coupling with different chemisorption species. Furthermore, we discuss potential applications of such nanochain-structured graphene as anisotropic quantum devices, based on calculations and analyses of their topological edge states and transport properties.
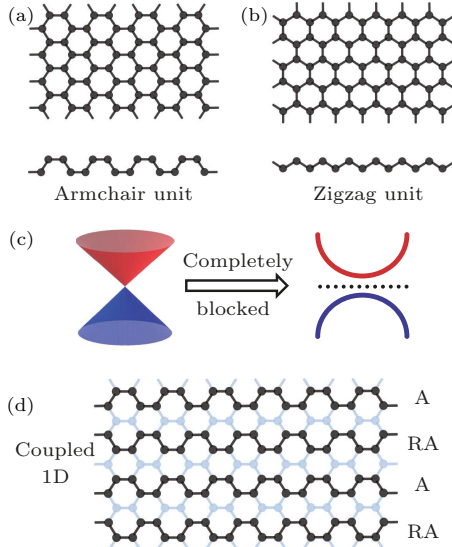
Fig. 1. Illustration of the top-down patterning of 2D graphene. (a) Armchair chain (AC) as the 1D building unit of graphene. (b) Zigzag chain as the 1D building unit of graphene. (c) Complete blocking the coupling between building units of graphene turns the relativistic Dirac fermions into ordinary fermions. (d) Schematic of partially blocking 2D graphene into patterned armchair-to-reversed-armchair (A–RA) chains. The tunable inter-AC coupling drives the system into different Dirac states without gap opening (see Fig. 3).

The concept of the proposed top-down patterning approach to create a nanostructured graphene platform is illustrated in Fig. 1. From reductionism, if one imagines graphene is made of 1D building blocks, then the smallest 1D unit is either an armchair, zigzag or chiral atomic chain in different ori-

entations. It is well known that the AC [Fig. 1(a)], which represents a 1D SSH model, is a semiconductor, while the zigzag chain [Fig. 1(b)] is an antiferromagnetic semiconductor.[13,43] Accordingly, it has been proposed before to nanopatterning graphene into a semiconductor. For example, by patterning graphene into a nanohole superlattice with both armchair and zigzag edges, a dilute magnetic semiconductor can be designed.[44] It is important to note that previous nanopatterning approach has generally assumed to completely block the hopping between the nanoscale building blocks,[45,46] which converts the relativistic Dirac fermions into ordinary non-relativistic fermions by opening a gap at the Dirac point [Fig. 1(c)]. Differently, using the 1D SSH ACs as the building blocks, here we propose to only partially block the inter-chain coupling [Fig. 1(d)], which retains the Dirac fermions without opening a gap but convert them into different types (Fig. 3). We achieve this partial blocking by selective surface adsorption, which makes it possible to tune the inter-chain coupling by using different adsorption species, as demonstrated below.
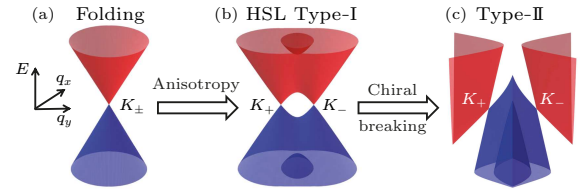
Fig. 2. Schematic illustration of Dirac cone tilting evolution by symmetry breaking. (a) Pristine folded Dirac cone of the honeycomb lattice. (b) Formation of high-symmetry line (HSL) Dirac cone upon introducing anisotropy, with $\delta_1 > m_1$, $\delta_2 = 0$, $|\tilde{v}_y| = 0$. (c) Type-II Dirac cone upon chiral (sublattice) symmetry breaking, with $\delta_1 > m_1$, $\delta_2 = 0$, $|\tilde{v}_y| > |v_y|$.

We first discuss the general working principle underlying our idea, based on continuum model and symmetry analysis. Without losing generality, we start from the effective Hamiltonian of graphene,

$$H(\boldsymbol{K}_\pm + \boldsymbol{k}) = \pm v_x k_x \sigma_x + v_y k_y \sigma_y, \qquad (1)$$

where $v_{x,y}$ is the Fermi velocity; $k_{x,y}$ is the wave vector; σ_i are Pauli matrices of sublattices. For convenience, one can fold Dirac points ($K_\pm$ valleys) from the corners of Brillouin zone to Γ point, as shown in Fig. 2(a), considering a hypothetical superlattice consisting of a periodic array of 1D ACs. In this stage, we neglect the inter-valley hybridization, and the superlattice Hamiltonian at Γ is

$$H_\Gamma^0(\boldsymbol{q}) = H(\boldsymbol{K}_+ + \boldsymbol{q}) \oplus H(\boldsymbol{K}_- + \boldsymbol{q})$$
$$= v_x q_x \tau_z \sigma_x + v_y q_y \tau_0 \sigma_y, \qquad (2)$$

where τ_i are Pauli matrices describing the valley pseudospin, $q_{x,y}$ is the wavevector measured from Γ point. Next, considering the coupled 1D system, it supports a two-fold rotational symmetry $C_{2y} : \tau_z \sigma_y$, and also preserves time-reversal $T : \tau_x K$ (K is a complex conjugation operator), inversion $P : \tau_x \sigma_x$, and mirror

M_{xz}: $\tau_y\sigma_z$ symmetries, as inherited from the original honeycomb lattice. The terms that respect all these symmetries include $m_1\tau_x\sigma_x$, $\delta_1\tau_z\sigma_y$ and $\delta_2\tau_y\sigma_z$. Here, $m_1\tau_x\sigma_x$ denotes the mass term arising from the $K_{\pm}$ valley hybridization when they are approaching, which would open a gap. We introduce $\delta_1\tau_z\sigma_y$ and $\delta_2\tau_y\sigma_z$ to account for the apparent anisotropy in the patterned lattice, which denote the different separations of the $K_{\pm}$ valleys in the q_x and q_y directions, respectively, due to the inter-valley interaction. The anisotropy requires $\delta_1 \neq \delta_2$ and their total strength acts as $\sqrt{|\delta_1^2 - \delta_2^2|}$ [see Fig. S8(a)]. For simplicity, we take $\delta_2 = 0$ so that δ_1 quantifies the degree of anisotropy. The greater the δ_1, the larger the anisotropy and separation of $K_{\pm}$ valleys. Combining $m_1\tau_x\sigma_x$ and $\delta_1\tau_z\sigma_y$, in order to preserve the Dirac cone, $\delta_1 > m_1$ must be satisfied, then the

type-I Dirac cone appears along the high-symmetry line (HSL) $q_x = 0$ with the $K_{\pm}$ valleys locating at $(0, \pm\sqrt{\delta_1^2 - m_1^2}/v_y)$, as shown in Fig. 2(b). Moreover, tilting of Dirac cone occurs because the Dirac point is not located at a high-symmetry point.[47] One can consider another $\tilde{v}_y|q_y|\tau_0\sigma_0$ term to break chiral (sublattice) symmetry $C: \tau_o\sigma_z$ while preserving T, P, C_{2y} and M_{xz} symmetries. Then the full $k\cdot p$ Hamiltonian is

$$H_\Gamma(\boldsymbol{q}) = v_x q_x \tau_z\sigma_x + v_y q_y \tau_0\sigma_y + m_1\tau_x\sigma_x$$
$$+ \delta_1\tau_z\sigma_y + \tilde{v}_y|q_y|\tau_0\sigma_0. \tag{3}$$

Equation (3) contains a critical point $|\tilde{v}_y| = |v_y|$ for the existence of type-III Dirac state. Therefore, the type-II Dirac cone emerges once $|\tilde{v}_y| > |v_y|$ is satisfied, as illustrated in Fig. 2(c).
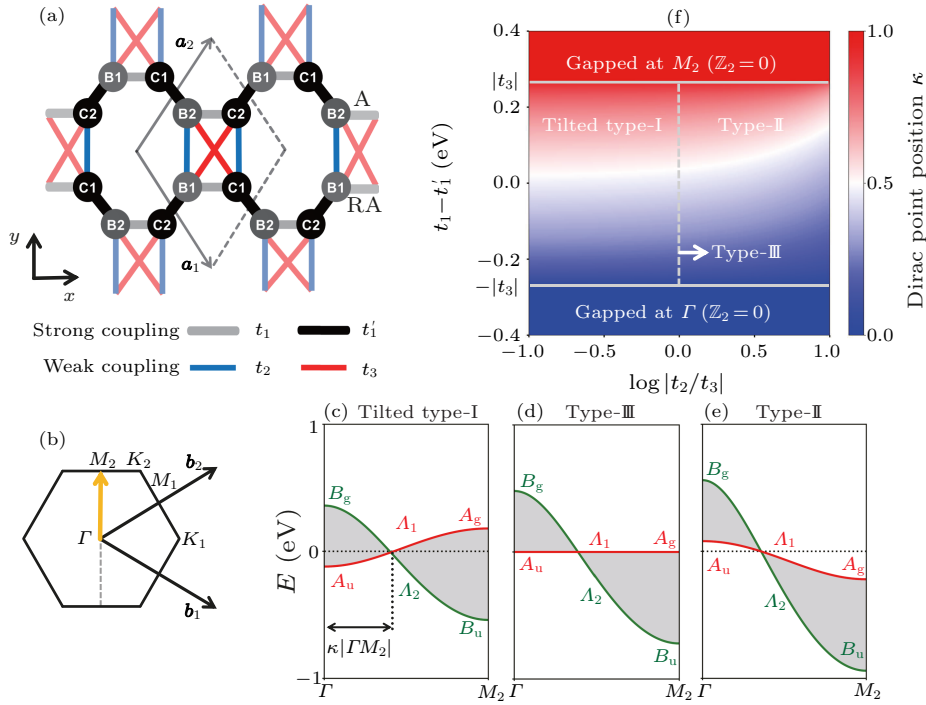
Fig. 3. Engineering Dirac cone in coupled 1D ACs. (a) Schematic of the A–RA-type coupled-chain model (CCM). The gray and black sites belong to different sublattices. (c) The first Brillouin zone. (c)–(e) Band structures of tilted type-I, type-III and type-II Dirac states, respectively, with fixed $t_1 = -1.90$, $t_1' = -1.96$, $t_3 = 0.3$: (c) $t_2 = -0.15$, $\Delta = -0.03$; (d) $t_2 = -0.3$, $\Delta = -0.06$; (e) $t_2 = -0.5$, $\Delta = -0.14$. The red (green) bands share $+1$ (-1) eigenvalues under C_{2y} operation. In (c)–(e), only two bands of interest are shown and all parameters are in units of eV. (f) Phase diagram with fixed $t_1' = -1.96$, $t_3 = 0.27$ and $\Delta = 0$. Here, the gray lines denote the boundary between Dirac and gapped states, the gray dashed line denotes type-III Dirac state. The Dirac point position κ is marked in (c) and $\kappa = 0$ (1) represents the gap location at Γ (M_2).

We then investigate the specific parametric conditions for engineering the Dirac phases in the nanochain-structured graphene by developing a coupled-chain model (CCM). We focus on the symmorphic armchair-to-reversed-armchair (A–RA) configuration, as shown in Fig. 3(a), and leave the results of the A–A configuration in Figs. S1 and S2 (see the Supplementary Material). The Wannier orbitals are p_z-like and the gray (black) dots mark the sublattice

B (C) sites. Then the four-site Hamiltonian is given by

$$H_0 = \sum_{\alpha i} \Delta_{\alpha i} c_{\alpha i}^\dagger c_{\alpha i} + \sum_{\langle\alpha i,\beta j\rangle_x} t_{\alpha i,\beta j}^x c_{\alpha i}^\dagger c_{\beta j}$$
$$+ \sum_{\substack{\langle\alpha i,\beta j\rangle_y \\ \langle\langle\alpha i,\beta j\rangle\rangle_y}} t_{\alpha i,\beta j}^y c_{\alpha i}^\dagger c_{\beta j} + \text{H.c.}, \tag{4}$$

where $\langle\,\rangle$ and $\langle\langle\,\rangle\rangle$ represent the nearest and next-nearest hopping, respectively; $\alpha, \beta = \text{B, C}$ and $i, j =$

1, 2; on-site energies $\Delta_{\alpha i}$ are uniformly set as Δ; $t^x_{\alpha i,\beta j}$ denotes intra-AC coupling t_1 and t'_1 along x direction, and $t^y_{\alpha i,\beta j}$ represents inter-AC coupling t_2 and t_3 along y direction. Note that the relatively weak inter-AC coupling is considered up to the next-nearest neighbor. CCM obeys time-reversal symmetry and C_{2h} point group symmetry. The spatial operators include two-fold rotation C_{2y} (B1→C1, B2→C2), mirror M_{xz} (B1→B2, C1→C2) and inversion P (B2→C1, B1→C2). Figures 3(c)–3(e) show the band structures of CCM, which illustrate the tilting of Dirac cone into tilted type-I, type-Ⅲ and type-Ⅱ Dirac in the coupled 1D ACs. The tilted Dirac cone elongates along the C_{2y} invariant Γ–M_2 path, which is characterized by a nontrivial time-reversal invariant[48,49] $\mathbb{Z}_2 = 1$ (see Table S1).

We have constructed a phase diagram of the resulting Dirac fermions in the parameter space of relative hopping strength, as shown in Fig. 3(f). At the limit of vanishing inter-AC coupling, i.e., $t_2 = t_3 = 0$, the CCM model reduces simply to the conventional SSH model, exhibiting a universal Peierls transition.[50] Given the intra-AC hopping $t_1 \neq t'_1$, there exists a 1D gap $\Delta_{1D} = 2|t_1 - t'_1|$.[51] With the inter-AC coupling, if $|t_3| > \Delta_{1D}/2$, the 2D Dirac state retains, albeit with an anisotropic and tilted Dirac cone; otherwise, the Dirac state disappears with a gap opening. Thus, the conditions $t_1 - t'_1 = \pm|t_3|$ set up two horizontal phase boundaries for the existence of Dirac fermions, as shown in Fig. 3(f). Inside these two boundaries, another vertical boundary conditioned with $|t_2| = |t_3|$ divides different types of Dirac fermions. Note that the inter-AC coupling t_2 breaks chiral (or bipartite lattice) symmetry. Since the Fermi velocity of one Dirac branch is proportional to $|t_2|-|t_3|$, it goes to zero when $|t_2| = |t_3|$, which gives rise to the type-Ⅲ Dirac fermions and divides the type-I ($|t_2|< |t_3|$) and type-Ⅱ ($|t_2|> |t_3|$) regions. The effect of spin-orbit coupling (SOC) and edge states of CCM are discussed in Figs. S3, S6 and S7.
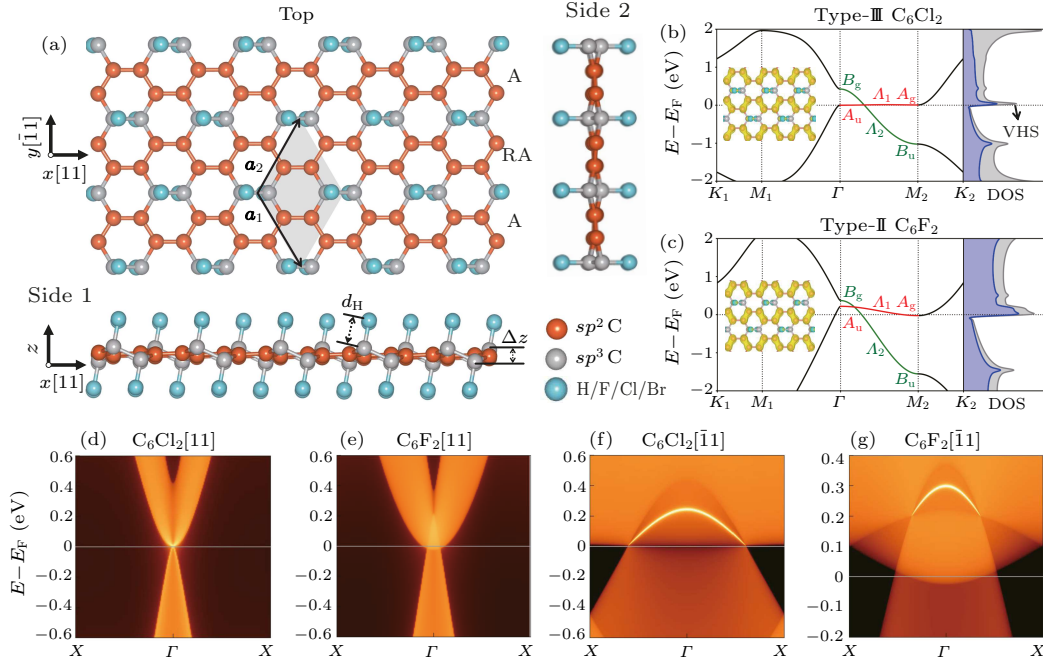
Fig. 4. Highly tilted Dirac fermions in the AC-patterned graphene. (a) Atomic structure of the AC-patterned graphene. The sp^2 carbons (orange) constitute the A–RA type chains. Bond lengths of C–X (d_H) are 1.11, 1.44, 1.87, 2.22 Å and sp^3 carbon buckling heights (Δz) are 0.67, 0.63, 0.63, 0.53 Å for X = H, F, Cl, Br, respectively. [(b), (c)] Spinless band structures with density of states (DOS) of C_6Cl_2 and C_6F_2, respectively. In (b) and (c), the red (green) bands share +1 (−1) eigenvalues under C_{2y} operation and total DOS (gray filled) near the Fermi level are mainly from p_z orbitals of sp^2 carbons (blue filled). The left insets are real-space charge distribution near the Fermi level. VHS is short for van Hove singularity. (d)–(g) Spinless semi-infinite spectra of C_6Cl_2 periodic along [11], C_6F_2 periodic along [11], C_6Cl_2 periodic along [$\bar{1}$1] and C_6F_2 periodic along [$\bar{1}$1], respectively. In (f) and (g), two helical edge states are degenerate.

Now, we propose material realization of the above CCM, namely a top-down nanopatterning process of graphene. Inspired by the fabrication of one-third hydrogenated graphene with long-range 1D AC patterns,[52] we devise a form of AC-patterned graphene in Fig. 4(a). One notices that the A–RA stacked sp^2 carbon ACs are staggered by sp^3 carbons. The unit formula of such AC-patterned graphene is C_6X_2 (X = H, F, Cl, Br). The lattice constants are 4.31, 4.30, 4.30, 4.31 Å for X = H, F, Cl, Br, respectively, and the lattice belongs to the layer group $C2/m$ with C_{2y}, M_{xz} and P operations. The phonon calculations confirm their dynamical stability (Fig. S10).

Figures 4(b) and 4(c) (see also Fig. S9) show the band structures of AC-patterned graphene, obtained from first-principles calculations, which clearly illus-

trate the phase transition of Dirac fermions. In particular, Fig. 4(b) displays the spinless type-Ⅲ Dirac fermion along the Γ–M_2 path for C_6Cl_2. One Dirac band branch is flat with a 13-meV bandwidth, leading to a van Hove singularity (VHS) in the density of states (DOS). The SOC opens a negligible gap of 2.0 meV. Figure 4(c) shows the type-Ⅱ Dirac fermion for C_6F_2, and the Dirac point is $\sim$0.2 eV above the Fermi level. The manipulated Dirac states in the AC-patterned graphene are found to be robust when placed on an insulating substrates, such as BN (0001) (see Figs. S13 and S14). We also discovered the existence of type-Ⅱ Dirac fermions in the AC-patterned silicene and strained germanene (Fig. S12). In addition, the first-principles results of AC-patterned graphene are well fitted by both CCM in Fig. S5 and maximally localized Wannier functions[53] in Fig. S11. The fitting parameters confirm quantitatively the phase diagram of CCM. For instance, the fitted parameters are $t_2 = -0.54$ eV and $t_3 = 0.42$ eV for C_6F_2, which satisfy the $|t_2| > |t_3|$ condition for the type-Ⅱ Dirac fermion.

Next, we study the edge states of AC-patterned graphene. We first evaluate the topological descriptors (see Table S2). The spinless semimetal phase of AC-patterned graphene is featured with crossings of bands with opposite C_{2y} eigenvalues. This gives rise to a nontrivial $\mathbb{Z}_2 = 1$ and rotation invariant $\delta_r = 1$ (as defined in Ref. [54]). Also, the 2D Zak phase[55] or electrical polarization[56] is calculated as $(p_1, p_2) = (0, 1/2)$, indicating a fractional topological charge $e/2$ along Γ–M_2 path. The directional edge band structures and semi-infinite edge spectra of AC-patterned graphene are shown in Figs. 4(d)–4(g) and Figs. S17–S21. We have considered the periodic directions of [10], [11] and [$\bar{1}$1] with different ribbon terminations. Here, we focus on the centrosymmetric ribbons along the C_{2h} preserving [11] and [$\bar{1}$1] directions. Along the [11] direction, two bulk Dirac cones of AC-patterned graphene are folded into the Γ point. In Figs. 4(d) and 4(e) of edge spectra, the conduction band dispersion of C_6F_2 and C_6Cl_2 becomes parabolic with a U shape. Due to the existence of $e/2$ topological charge along [$\bar{1}$1] direction, we observe two degenerate helical modes within the bulk states of C_6F_2 and C_6Cl_2 [Figs. 4(f) and 4(g)]. The helical modes come in pairs subjected to the C_{2y} rotation symmetry.

To further explore the transport properties of AC-patterned graphene, we calculate the static conductivity tensor using the Kubo–Bastin formula based on linear response theory:[57,58]

$$\sigma_{\alpha\beta}(\mu, T) = \frac{ie^2\hbar}{\Omega} \int_{-\infty}^{\infty} d\varepsilon f(\varepsilon) \times \mathrm{Tr}\Big[\nu_\alpha \delta(\varepsilon - H)\nu_\beta$$
$$\cdot \frac{dG^+(\varepsilon, H)}{d\varepsilon} - \nu_\alpha \frac{dG^-(\varepsilon, H)}{d\varepsilon}\nu_\beta \delta(\varepsilon - H)\Big], \quad (5)$$

where T is temperature, μ is chemical potential, Ω is the volume of primitive cell, $\nu_{\alpha,\beta}$ is the velocity

operator, $f(\varepsilon)$ is the Fermi–Dirac distribution and $G^\pm(\varepsilon, H) = [(\varepsilon - H \pm i\eta)]^{-1}$ are the advanced $(+)$ and retarded $(-)$ Green's functions. In Fig. 5, we compare the conductivities of AC-patterned graphene with graphene at 0 K. First, the coupled ACs display a larger longitudinal conductivity σ_{xx} along the chain direction than graphene, while the "barrier" from sp^3 carbons in between the ACs limits the electron transport in the y-direction. The high anisotropy manifests a distinct quasi 1D electrical response in AC-patterned graphene. Second, there exist significant conductivity differences between type-I (graphene), tilted type-I (C_6H_2), type-Ⅲ (C_6Cl_2) and type-Ⅱ (C_6F_2) Dirac fermions. In particular, σ_{xx} of C_6F_2 (C_6Cl_2) is as high as 21.9 e^2/h (17.8 e^2/h) at Fermi level, indicating that the highly tilted Dirac fermions endow C_6F_2 (C_6Cl_2) with metallic behavior, distinct from the semimetal graphene or C_6H_2. Consequently, C_6F_2 and C_6Cl_2 are promising for designing highly anisotropic quantum devices with x-directional transport and y-directional topological edge conductance.
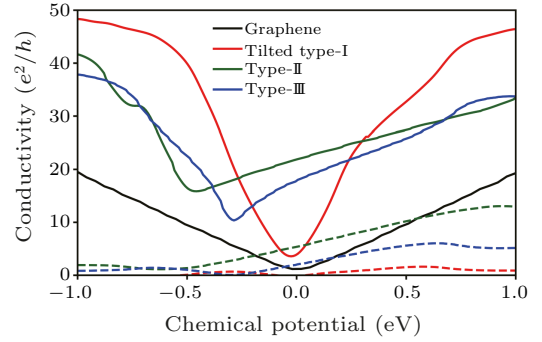
Fig. 5. Kubo–Bastin static conductivity of tilted type-I C_6H_2 (red), type-Ⅱ C_6F_2 (green), type-Ⅲ C_6Cl_2 (blue) and graphene (black) at 0 K. The solid and dashed lines are longitudinal σ_{xx} and σ_{yy} tensor components, respectively, which are degenerate for graphene.

In conclusion, we have theoretically investigated a top-down nanopatterning approach of 2D graphene to manipulate the Dirac fermions, such as changing from isotropic type-I to anisotropic type-Ⅱ and type-Ⅲ. Our model analyses and material calculations extend the study of topological states to coupled 1D systems, which links the 1D SSH model with the 2D Kane–Mele model.[48,59] Furthermore, we demonstrate the concept of nanopatterning in reconstructing a pristine system with novel functionality by selective chemisorption. It is worth noting that one of our proposed nanochain-structured graphene, namely C_6H_2 monolayer, has already been successfully fabricated in millimeter scale using ultrahigh vacuum radio frequency plasma.[52] Similar plasma methods are promising for synthesizing halogenated graphene C_6F_2, C_6Cl_2 via halogenating agents such as XeF_2[60] and Cl_2[61] under suitable conditions of plasma concentration, treatment time, and substrate, etc. These results enrich the fundamental understanding of 2D Dirac fermions and provide guidance for designing

functional nanostructures based on graphene, and therefore, are expected to draw immediate attention from experimentalists.

References

[1] Novoselov K S, Geim A K, Morozov S V, Jiang D, Zhang Y, Dubonos S V, Grigorieva I V and Firsov A A 2004 *Science* **306** 666

[2] Novoselov K S, Geim A K, Morozov S V, Jiang D, Katsnelson M I, Grigorieva I V, Dubonos S V and Firsov A A 2005 *Nature* **438** 197

[3] Liu Z K, Zhou B, Zhang Y, Wang Z J, Weng H M, Prabhakaran D, Mo S- K, Shen Z X, Fang Z, Dai X, Hussain Z and Chen Y L 2014 *Science* **343** 864

[4] Lv B Q, Weng H, Fu B B, Wang X P, Miao H, Ma J, Richard P, Huang X, Zhao L and Chen G 2015 *Phys. Rev. X* **5** 031013

[5] Soluyanov A A, Gresch D, Wang Z J, Wu Q S, Troyer M, Dai X and Bernevig B A 2015 *Nature* **527** 495

[6] Bzdušek T, Wu Q, Rüegg A, Sigrist M and Soluyanov A A 2016 *Nature* **538** 75

[7] Wang Z, Alexandradinata A, Cava R J, Bernevig B A 2016 *Nature* **532** 189

[8] Zhu Z, Winkler G W, Wu Q, Li J and Soluyanov A A 2016 *Phys. Rev. X* **6** 031003

[9] Stenull O, Kane C and Lubensky T 2016 *Phys. Rev. Lett.* **117** 068001

[10] Gusynin V and Sharapov S 2005 *Phys. Rev. Lett.* **95** 146801

[11] Zhang Y, Tan Y W, Stormer H L and Kim P 2005 *Nature* **438** 201

[12] Beenakker C 2008 *Rev. Mod. Phys.* **80** 1337

[13] Son Y W, Cohen M L and Louie S G 2006 *Nature* **444** 347

[14] Nomura K and MacDonald A H 2007 *Phys. Rev. Lett.* **98** 076602

[15] Wu X, Li X, Zhang R Y, Xiang X, Tian J, Huang Y, Wang S, Hou B, Chan C T and Wen W 2020 *Phys. Rev. Lett.* **124** 075501

[16] Ozawa T, Price H M, Amo A, Goldman N, Hafezi M, Lu L, Rechtsman M C, Schuster D, Simon J, Zilberberg O and Carusotto I 2019 *Rev. Mod. Phys.* **91** 015006

[17] Noh H J, Jeong J, Cho E J, Kim K, Min B and Park B G 2017 *Phys. Rev. Lett.* **119** 016401

[18] Yan M, Huang H, Zhang K, Wang E, Yao W, Deng K, Wan G, Zhang H, Arita M and Yang H 2017 *Nat. Commun.* **8** 257

[19] Huang H Q, Jin Y W and Liu F 2018 *Phys. Rev. B* **98** 121110(R)

[20] Sadhukhan K, Politano A and Agarwal A 2020 *Phys. Rev. Lett.* **124** 046803

[21] Teknowijoyo S, Jo N H, Scheurer M S, Tanatar M A, Cho K, Bud'ko S L, Orth P P, Canfield P C and Prozorov R 2018 *Phys. Rev. B* **98** 024508

[22] Fu B B, Yi C J, Wang Z J, Yang M, Lv B Q, Gao X, Li M, Huang Y B, Weng H M and Shi Y G 2019 *Chin. Phys. B* **28** 037103

[23] Liu H, Sun J T, Song C, Huang H, Liu F and Meng S 2020 *Chin. Phys. Lett.* **37** 067101

[24] Fei F, Bo X, Wang R, Wu B, Jiang J, Fu D, Gao M, Zheng H, Chen Y and Wang X 2017 *Phys. Rev. B* **96** 041201

[25] Burkov A 2018 *Phys. Rev. Lett.* **120** 016603

[26] Liu Y, Wang G, Huang Q, Guo L and Chen X 2012 *Phys. Rev. Lett.* **108** 225505

[27] Malko D, Neiss C, Vines F and Görling A 2012 *Phys. Rev. Lett.* **108** 086804

[28] Zhou X F, Dong X, Oganov A R, Zhu Q, Tian Y and Wang H T 2014 *Phys. Rev. Lett.* **112** 085502

[29] Gao H and Ren W 2020 *Carbon* **158** 210

[30] Gong Z, Shi X, Li J, Li S, He C, Ouyang T, Zhang C, Tang C and Zhong J 2020 *Phys. Rev. B* **101** 155427

[31] Cai J, Ruffieux P, Jaafar R, Bieri M, Braun T, Blankenburg S, Muoth M, Seitsonen A P, Saleh M and Feng X 2010 *Nature* **466** 470

[32] Huang M, Boone C, Roberts M, Savage D E, Lagally M G, Shaji N, Qin H, Blick R, Nairn J A and Liu F 2005 *Adv. Mater.* **17** 2860

[33] Roth W J, Nachtigall P, Morris R E, Wheatley P S, Seymour V R, Ashbrook S E, Chlubná P, Grajciar L, Položij M and Zukal A 2013 *Nat. Chem.* **5** 628

[34] Autès G, Isaeva A, Moreschini L, Johannsen J C, Pisoni A, Mori R, Zhang W, Filatova T G, Kuznetsov A N and Forró L 2016 *Nat. Mater.* **15** 154

[35] Noguchi R, Takahashi T, Kuroda K, Ochi M, Shirasawa T, Sakano M, Bareille C, Nakayama M, Watson M and Yaji K 2019 *Nature* **566** 518

[36] Noguchi R, Kobayashi M, Jiang Z, Kuroda K, Takahashi T, Xu Z, Lee D, Hirayama M, Ochi M and Shirasawa T 2021 *Nat. Mater.* **20** 473

[37] Yang T, Wan Q, Yan D, Zhu Z, Wang Z, Peng C, Huang Y, Yu R, Hu J and Mao Z 2020 *Nat. Mater.* **19** 27

[38] Wang B, Xia W, Li S, Wang K, Yang S A, Guo Y and Xue J 2021 *ACS Nano* **15** 7149

[39] Li Y, Dietrich S, Forsythe C, Taniguchi T, Watanabe K, Moon P and Dean C R 2021 *Nat. Nanotechnol.* **16** 525

[40] Bykov M, Fedotenko T, Chariton S, Laniel D, Glazyrin K, Hanfland M, Smith J S, Prakapenka V B, Mahmood M F and Goncharov A F 2021 *Phys. Rev. Lett.* **126** 175501

[41] Su W P, Schrieffer J and Heeger A J 1979 *Phys. Rev. Lett.* **42** 1698

[42] Su W P, Schrieffer J and Heeger A 1980 *Phys. Rev. B* **22** 2099

[43] Son Y W, Cohen M L and Louie S G 2006 *Phys. Rev. Lett.* **97** 216803

[44] Yu D, Lupton E M, Liu M, Liu W and Liu F 2008 *Nano Res.* **1** 56

[45] Balog R, Jørgensen B, Nilsson L, Andersen M, Rienks E, Bianchi M, Fanetti M, Lægsgaard E, Baraldi A and Lizzit S 2010 *Nat. Mater.* **9** 315

[46] Elias D C, Nair R R, Mohiuddin T, Morozov S, Blake P, Halsall M, Ferrari A C, Boukhvalov D, Katsnelson M and Geim A 2009 *Science* **323** 610

[47] Goerbig M O, Fuchs J N, Montambaux G and Piechon F 2008 *Phys. Rev. B* **78** 045415

[48] Kane C L and Mele E J 2005 *Phys. Rev. Lett.* **95** 146802

[49] Qi X L, Hughes T L and Zhang S C 2008 *Phys. Rev. B* **78** 045302

[50] Lee P A, Rice T and Anderson P 1973 *Phys. Rev. Lett.* **31** 462

[51] Gröning O, Wang S, Yao X, Pignedoli C A, Barin G B, Daniels C, Cupo A, Meunier V, Feng X and Narita A 2018 *Nature* **560** 209

[52] Chen H, Bao D L, Wang D F, Que Y D, Xiao W D, Qian G J, Guo H, Sun J T, Zhang Y Y, Du S X, Pantelides S T and Gao H J 2018 *Adv. Mater.* **30** 1801838

[53] Marzari N and Vanderbilt D 1997 *Phys. Rev. B* **56** 12847

[54] Song Z, Zhang T, Fang Z and Fang C 2018 *Nat. Commun.* **9** 3530

[55] Liu F and Wakabayashi K 2017 *Phys. Rev. Lett.* **118** 076803

[56] Liu F, Deng H Y and Wakabayashi K 2019 *Phys. Rev. Lett.* **122** 086804

[57] Bastin A, Lewiner C, Betbeder-Matibet O and Nozieres P 1971 *J. Phys. Chem. Solids* **32** 1811

[58] García J H, Covaci L and Rappoport T G 2015 *Phys. Rev. Lett.* **114** 116602

[59] Kane C L and Mele E J 2005 *Phys. Rev. Lett.* **95** 226801

[60] Robinson J T, Burgess J S, Junkermeier C E, Badescu S C, Reinecke T L, Perkins F K, Zalalutdniov M K, Baldwin J W, Culbertson J C and Sheehan P E 2010 *Nano Lett.* **10** 3001

[61] Wu J, Xie L, Li Y, Wang H, Ouyang Y, Guo J and Dai H 2011 *J. Am. Chem. Soc.* **133** 19668

Supplementary Material for

Manipulation of Dirac Fermions in

Nanochain-structured Graphene

Wen-Han Dong(董文翰)[1†], De-Liang Bao(包德亮)[1†], Jia-Tao Sun(孙家涛)[2*],

Feng Liu(刘峰)[3], and Shixuan Du(杜世萱)[1,4,5**]

[1]*Institute of Physics and University of Chinese Academy of Sciences, Chinese Academy of Sciences, Beijing 100190, China*
[2]*School of Information and Electronics, MIIT Key Laboratory for Low-Dimensional Quantum Structure and Devices, Beijing Institute of Technology, Beijing 100081, China*
[3]*Department of Materials Science and Engineering, University of Utah, Salt Lake City, Utah 84112, United States*
[4]*CAS Center for Excellence in Topological Quantum Computation, Beijing 100190, China*
[5]*Songshan Lake Materials Laboratory, Dongguan 523808, China*
[†]*These authors contributed equally*
*Correspondence to: jtsun@bit.edu.cn; **Correspondence to: sxdu@iphy.ac.cn*

This file contains:
1. **Methods**
2. **CCM Discussions**
3. **CCM Edge States**
4. $k \cdot p$ **Hamiltonian**
5. **First-Principles Results**
6. **External Response of AC-Patterned Graphene**
7. **Edge Bands of AC-Patterned Graphene**
8. **Edge Spectra of AC-Patterned Graphene**
9. **Band Irreducible Representations**

1. Methods

We performed first-principles calculations via Vienna Ab-initio Simulation Package[1] within density functional theory. The Perdew-Bruke-Ernzerhof parametrization[2] of generalized gradient approximation was adopted. All the energy cutoffs of plane-wave basis were set as 500 eV. A k-mesh of $20 \times 20 \times 1$ and another $16 \times 16 \times 1$ were used for Brillouin zone sampling of primitive cell and rectangular conventional unit cell, respectively. A dense k-mesh of $200 \times 200 \times 1$ was employed for calculating the density of states (DOS). The convergence conditions were 10^{-6} eV for total energy and 0.01 eV/Å for the atomic force, respectively. The thickness of vacuum layer was 15 Å. The phonon dispersions were acquired by using the density functional perturbation theory as coded in QUANTUM-ESPRESSO package,[3] using a $18 \times 18 \times 1$ k-mesh and a $3 \times 3 \times 1$ q-mesh. We constructed the maximally localized Wannier functions (MLWFs)[4] from p_z orbitals of sp^2 hybridized carbons via Wannier90 code.[5] The Kubo optical conductivity tensor was computed using Kubo-Greenwood formula and a $200 \times 200 \times 1$ k-mesh. The edge band structures of nanoribbons were calculated using Hamiltonian constructed from MLWFs. The spectral functions were calculated using the iterative Green's function technique[6] as implemented in the WannierTools package.[7] The Kubo-Bastin conductivities were calculated using Chebyshev polynomial[8] with tight-binding fitted Hamiltonian, where we adopted -2.8 eV as the nearest-neighbor hopping of graphene.

We obtained quantized dipole in 2D systems with inversion and time-reversal

symmetry by:[9]

$$p_i = \frac{1}{2}\left(\sum_{n \in occ} q_i^n \text{ modulo } 2\right), \quad (-1)^{q_i^n} = \frac{\eta^n(M_i)}{\eta^n(\Gamma)} \tag{S1}$$

where i = 1 or 2 denotes the direction of reciprocal lattice vector; $\eta^n(k)$ is parity eigenvalue of the nth occupied band at k point.

2. CCM Discussions

The A-A type coupled-chain models (CCMs) have non-symmorphic structures as shown in Fig. S1(a) and Fig. S2(a), as generated from honeycomb or rectangular lattices. Up to the next nearest-neighbor (NN) interchain chain coupling, the A-A type CCMs exhibit Dirac cone when $|t_2| > |t_1 - t_1'|$. The Dirac cone tunability of A-A type CCM is similar to the A-RA type, with $|t_2| = |t_3|$ as the critical condition for type-III Dirac cone. We further considered the third-NN interchain coupling due to the lattice geometry, type-II Dirac cone also appears in Fig. S1(d). However, the critical condition for type-III Dirac cone becomes complicated because one of the Dirac band is not completely flat as the third-NN interchain coupling is included.

3
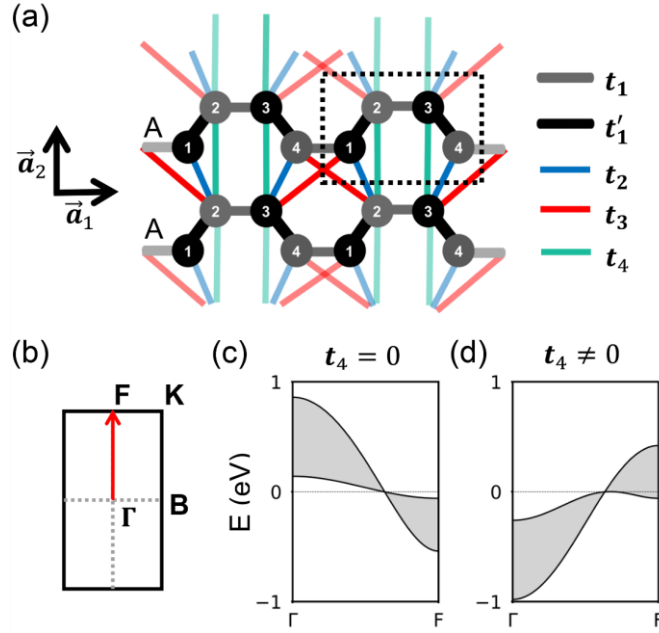
Fig. S1. A-A type CCM in a honeycomb lattice. (a) Structure schematic. Here, strong intrachain x couplings are t_1 and t_1', weak interchain y couplings are t_2, t_3 and t_4. (b) First Brillouin zone. (c) Band structure of type-II Dirac cone with $t_1 = -1.9$ eV, $t_1' = -1.96$ eV, $t_2 = -0.3$ eV, $t_3 = -0.4$ eV and $\Delta= 0.1$ eV. (d) Band structure of type-II Dirac cone with $t_1 = -1.9$ eV, $t_1' = -1.96$ eV, $t_2 = -0.3$ eV, $t_3 = -0.4$ eV, $t_4 = -0.4$ eV and $\Delta= -0.22$ eV.
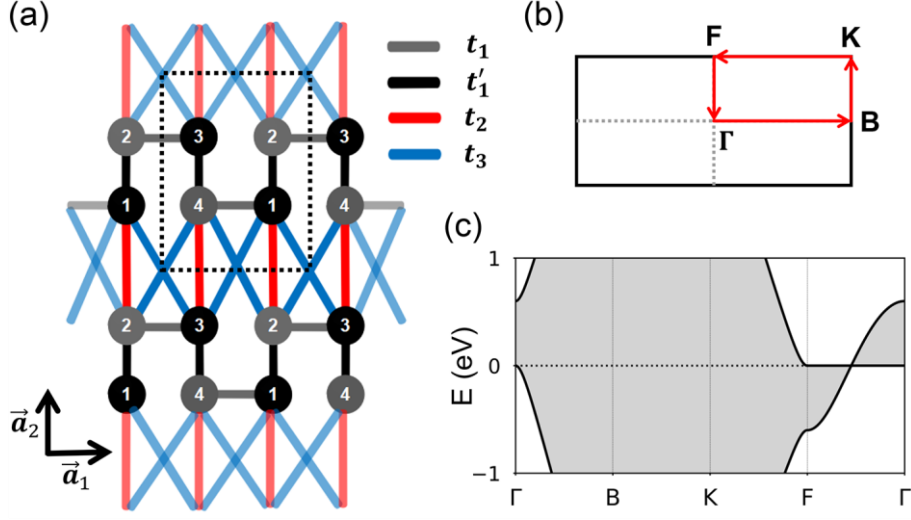
Fig. S2. A-A type CCM in a rectangular lattice. (a) Structure schematic. (b) First Brillouin zone. (c) Band structure of type-III Dirac cone. Here, $t_1 = t_1' = -1.96$ eV, $t_2 = -0.3$ eV, $t_3 = -0.15$ eV and $\Delta= 0$ eV. The critical condition for type-III Dirac cone with flat band is $|t_2| = 2|t_3|$.

Next, we investigated the spin-orbit coupling (SOC) effect of CCM, i.e., $H = H_0 + H_{soc}$ (H_0 is given in Eq. (4)). The leading SOC term for A-RA type CCM is

$$H_{soc} = \sum_{<\alpha i, \beta j >_y} i\lambda_{so} v_{\alpha i, \beta j} c_{\alpha i}^{\dagger} s^z c_{\beta j} + H.c. \tag{S2}$$

where λ_{so} is the strength of Kane-Mele[10] like SOC; $v_{\alpha i, \beta j} = (2/\sqrt{3}) (\hat{d}_{\alpha i} \times \hat{d}_{\beta j})_z = \pm 1$; s^z is the spin Pauli matrix. The SOC term will open a gap at Dirac point.

4

Here, we considered the same next-NN SOC as in the low-buckled silicene[11,12] because the sp^3 carbons of monolayer C_6X_2 (X = H, F, Cl, Br) in Fig. 3(a) cause atomic buckling.
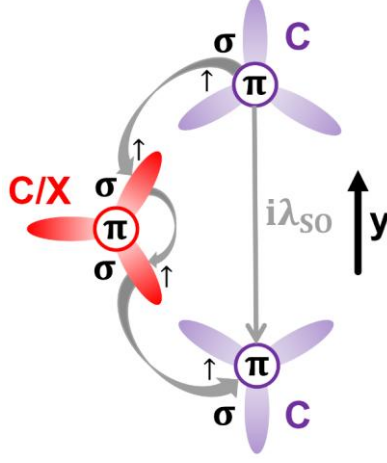
Fig. S3. Schematic of the leading SOC term in A-RA type CCM.

To better understand the Dirac cone in CCM, the symmetry protection of Dirac cone is discussed in Fig. S4. The first-principles fitted band structures in Fig. S5 show that the A-RA type CCM with up to next-NN interchain coupling is sufficient to describe the highly tilted Dirac cones in armchair-chain (AC) patterned graphene.
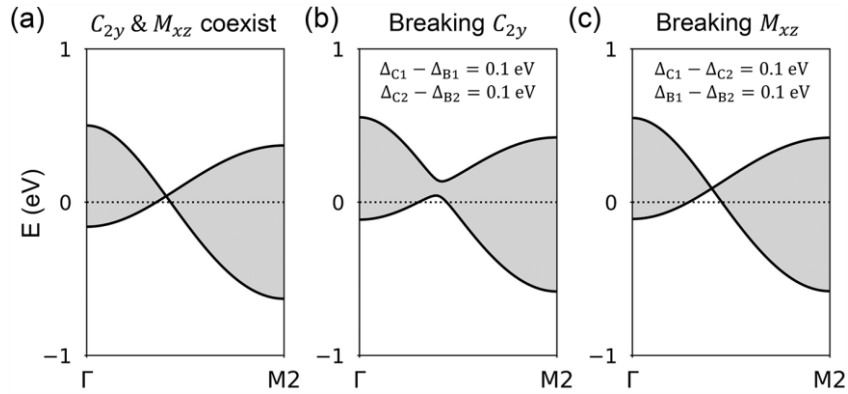
Fig. S4. Two-fold rotation C_{2y} protected Dirac cones in A-RA type CCM. (a,c) The nontrivial band crossings rely on the existence of C_{2y}. (b) The gapped insulator phase will emerge once C_{2y} is broken while preserving M_{xz}. Corresponding t_1, t_1', t_2 and t_3 in (a-c) are -2.275, -2.36, -0.15 and 0.415 eV, respectively.
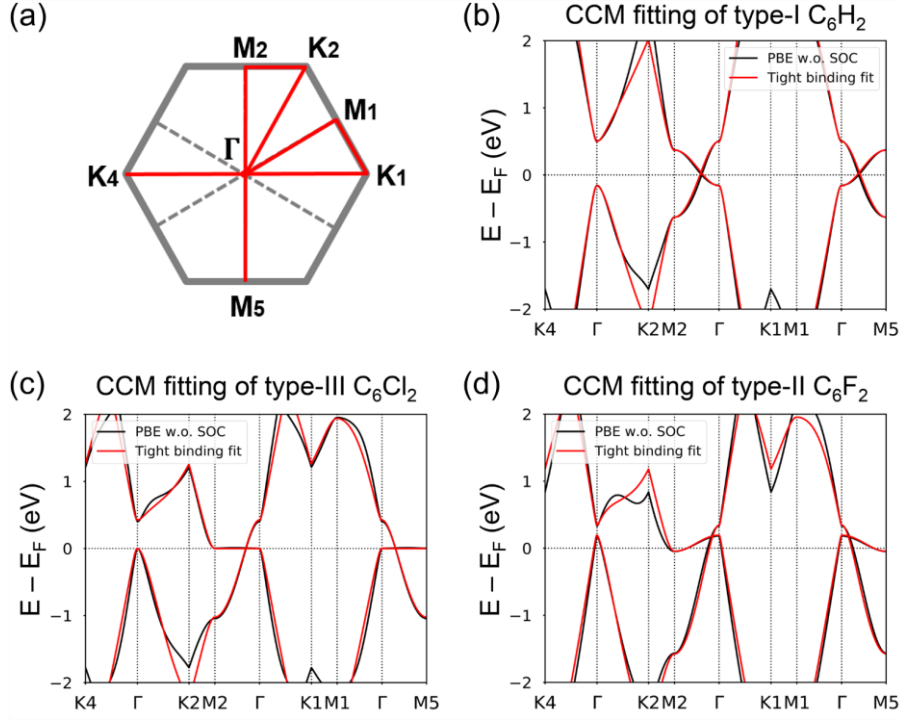
Fig. S5. (a) High-symmetry k-path. (b-d) The A-RA type CCM bands fitted to the first-principles bands for monolayer C_6H_2, C_6Cl_2 and C_6F_2, respectively. In (b), t_1, t_1', t_2, t_3 and Δ equal to -2.275, -2.36, -0.15, 0.415 and 0.02 eV, respectively ; In (c), t_1, t_1', t_2, t_3 and Δ equal to -1.82, -1.97, -0.362, 0.362 and -0.15 eV, respectively; In (d), t_1, t_1', t_2, t_3 and Δ equal to -1.915, -2.26, -0.54, 0.42 and -0.27 eV., respectively.

3. CCM Edge States

   The edge states of A-RA type CCM are examined with considering SOC effect. Two pairs of helical modes branch out from the bulk states, as in Fig. S7.
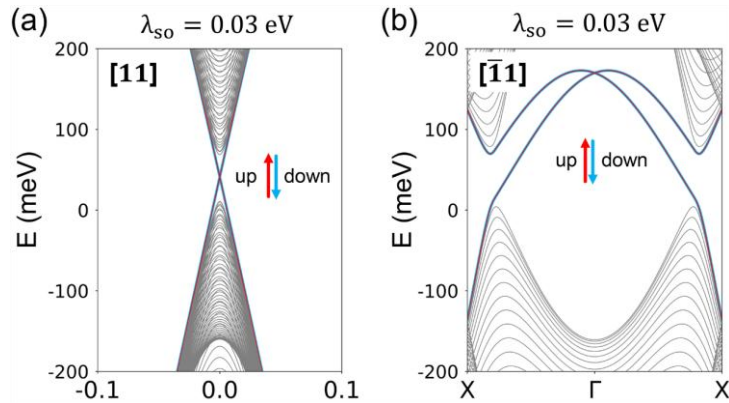
Fig. S6. Predicted tilted type-I edge bands of A-RA type CCM with $\lambda_{so} = 0.03$ eV. (a) $N = 60$ and periodic along x direction. (b) $N = 200$ and periodic along y direction. In both (a) and (b), t_1, t_1', t_2, t_3 and Δ equal to -2.275, -2.36, -0.15, 0.415 and 0 eV, respectively. The abscissa is in units of $\frac{2\pi}{L}$ and N is relative ribbon width.

(a) $t_1, t_1' < 0; \lambda_{so} = 0$ eV (b) $t_1, t_1' < 0; \lambda_{so} = 0.03$ eV (c) $t_1, t_1' > 0; \lambda_{so} = 0.03$ eV
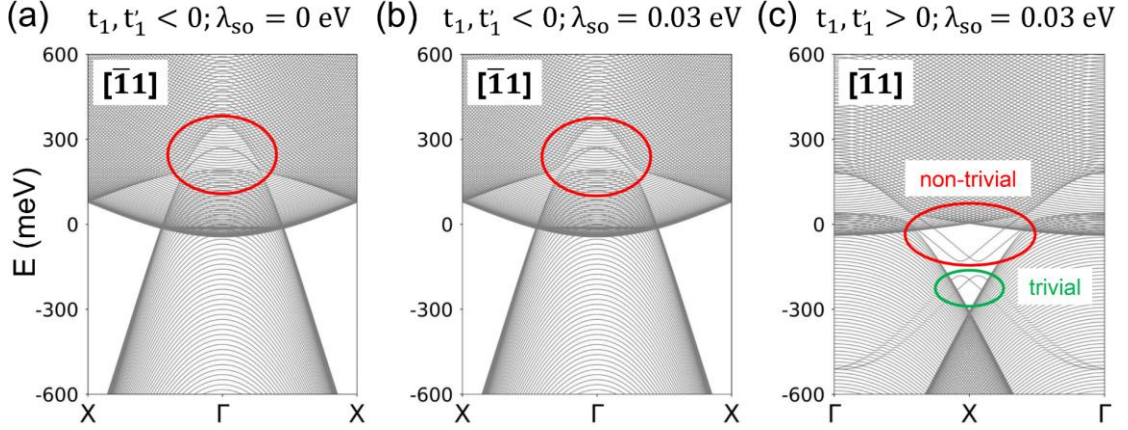
Fig. S7. Predicted type-II edge band structures of A-RA type CCM with $N = 200$ and $\lambda_{so} = 0$ eV. (a,b) t_1, t_1', t_2, t_3 and Δ equal to -1.915, -2.26, -0.54, 0.42 and -0.27 eV, respectively. (c) t_1, t_1', t_2, t_3 and Δ equal to 1.90, 1.70, -0.31, 0.27 and -0.20 eV, respectively. The helical modes in (a) are typically flat. Topological trivial modes from localized states (green) emerge in (c). In (b) and (c), up and down spin channels are degenerate.

4. $\boldsymbol{k} \cdot \boldsymbol{p}$ Hamiltonian

We also investigated the $\boldsymbol{k} \cdot \boldsymbol{p}$ Hamiltonian for other situations other than Fig. 2. For example, when valley hybridization $m_1 = 0$, the anisotropy ($\delta_1 > \delta_2 \neq 0$) also introduces splitting of Dirac cone (Fig. S8(a)). If none of m_1, δ_1 and δ_2 is zero, the chiral symmetry of $H_\Gamma(\boldsymbol{q})$ is slightly broken and the condition for Dirac cone along q_y direction becomes $\delta_1^2 > m_1^2 + \delta_2^2$ (Fig. S8(b)). Furthermore, when a SOC term $\lambda_{so}\tau_z\sigma_z s_z$ is considered, the Dirac cone becomes massive (s_z is the spin Pauli matrix).

7
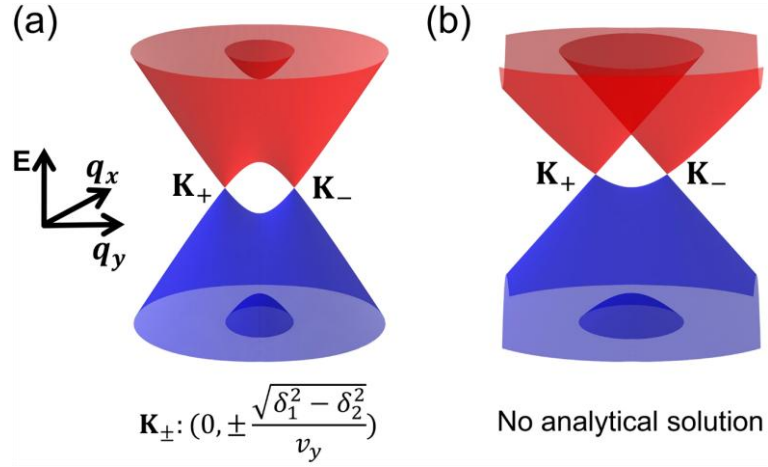
Fig. S8. $k \cdot p$ Hamiltonian Dirac cone schematics for (a) $m_1 = 0$, $\delta_1 > \delta_2 \neq 0$, $|\widetilde{v_y}| = 0$ and (b) $\delta_1^2 > m_1^2 + \delta_2^2$, $|\widetilde{v_y}| = 0$ with $m_1, \delta_1, \delta_2 \neq 0$.

5. First-Principles Results
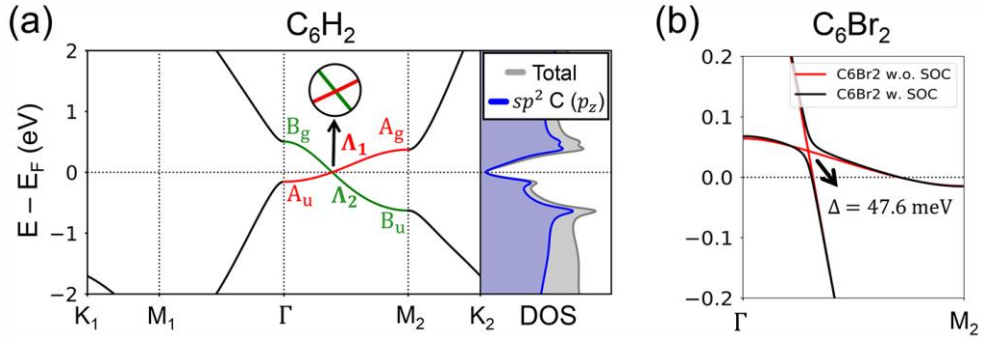
Fig. S9. (a) Spinless band structure with DOS of tilted type-I C_6H_2. The SOC gap is 0.9 meV. (b) Band structures of type-II C_6Br_2. The heavy element bromine introduces a considerable SOC that opens a 47.6 meV local energy gap (i.e., minimal gap at the same momentum). The system is overall metallic since it is globally gapless.
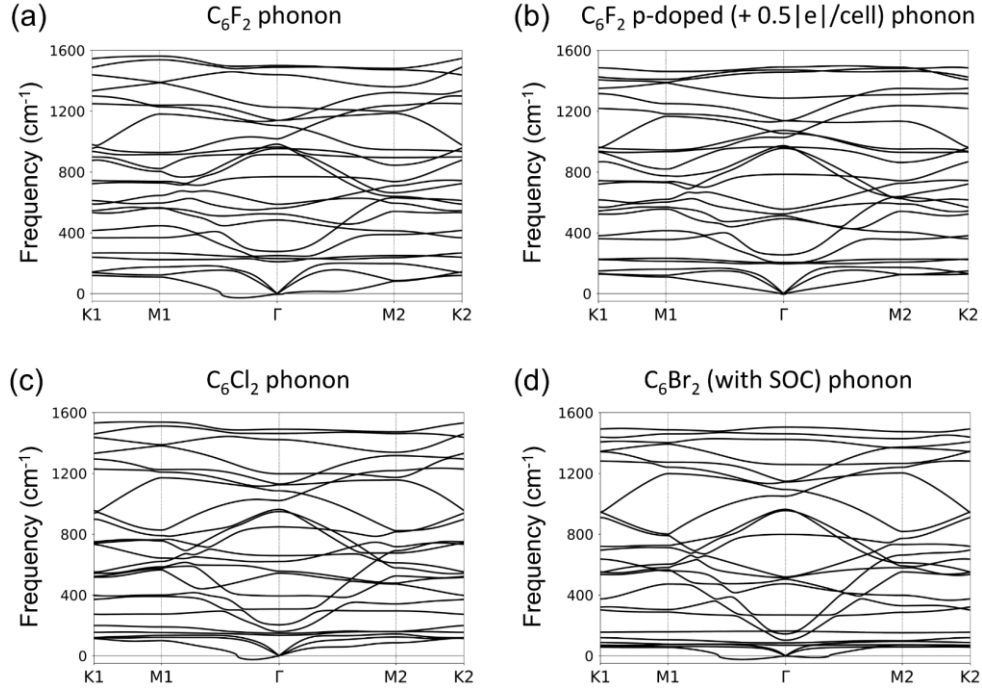
Fig. S10. The phonon spectra of C_6X_2 (X = F, Cl, Br). (a-d) Phonon dispersions of monolayer freestanding C_6F_2, hole doped C_6F_2, C_6Cl_2 and C_6Br_2, respectively. The phonon dispersion of C_6H_2 was reported dynamically stable [13].
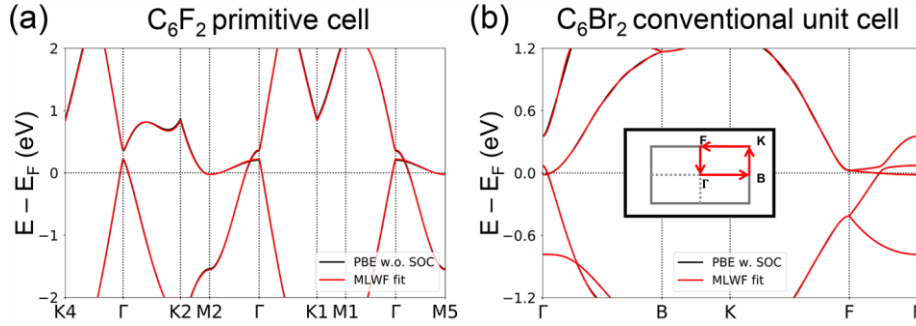
Fig. S11. The comparison of first-principles and MLWF fitted band structures. (a) C_6F_2 under a primitive cell without SOC and (b) C_6Br_2 under a conventional unit cell with SOC. The inset of (b) exhibits the Brillouin zone of (rectangular) conventional unit cell. The conventional unit cell allows additional screw axes 2_{1y} such that there are band crossings around Fermi level even with considering SOC in (b).

9

To validate the generality of our top-down approach of AC patterning for creating highly tilted Dirac fermions, we investigated other AC-patterned group-IV monolayers, as shown in Fig. S12(a-c). For AC-patterned group-V hexagonal monolayer structures such as Bi_6H_2 in Fig. S12(d), the electronic states at Fermi level are contributed by both $p_{x,y}$ and p_z orbitals of bismuth with SOC inverted bands, exhibiting the typical 2D topological insulator (TI) feature other than Dirac states.
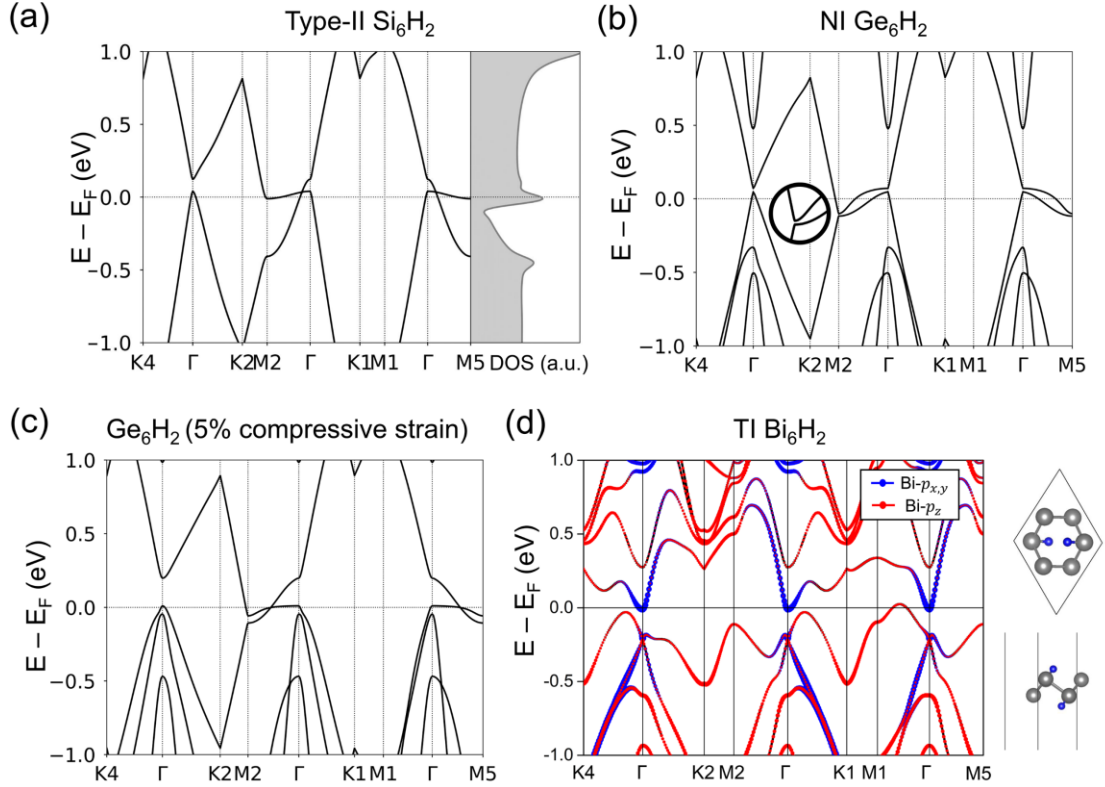
Fig. S12. (a) Band structure and DOS of AC-patterned silicene Si_6H_2 without SOC. The local energy gap with SOC is 7.0 meV. (b) Band structure of AC-patterned germanene Ge_6H_2 without SOC. The bands near Fermi level along Γ-M_2 path are tilted while there exist no Dirac cones, making Ge_6H_2 a normal insulator (NI). (c) Band structure of Ge_6H_2 under 5% y direction compressive strain without SOC. Type-II Dirac fermions emerge along Γ-M_2 path. (d) Band structure of Bi_6H_2 with SOC. The right panels show the buckled atomic structure.

We also investigated the robustness of the AC-patterned graphene on substrates.

The electronic states of monolayer C_6F_2 (type-II Dirac fermions) on the semiconducting BN (0001) substrate (4 layers) and metallic Ru (0001) substrate (3 layers) are shown in Fig. S13 and Fig. S14, respectively, with considering the surface relaxations and vdW-D3 correction.[14] In Fig. S13, the type-II Dirac fermions of C_6F_2 retain and are separatable from the BN substate in band structure. In Fig. S14, the surface Ru atoms couple strongly with the bottom-face F atoms of C_6F_2. The superlattice potential rearranges the bottom-face F atoms dramatically, while the metallicity of C_6F_2 is preserved, as indicated by the projected DOS in Fig. S14(c). In brief, the semiconducting BN substrate is favorable for supporting the pristine type-II Dirac fermions of C_6F_2.
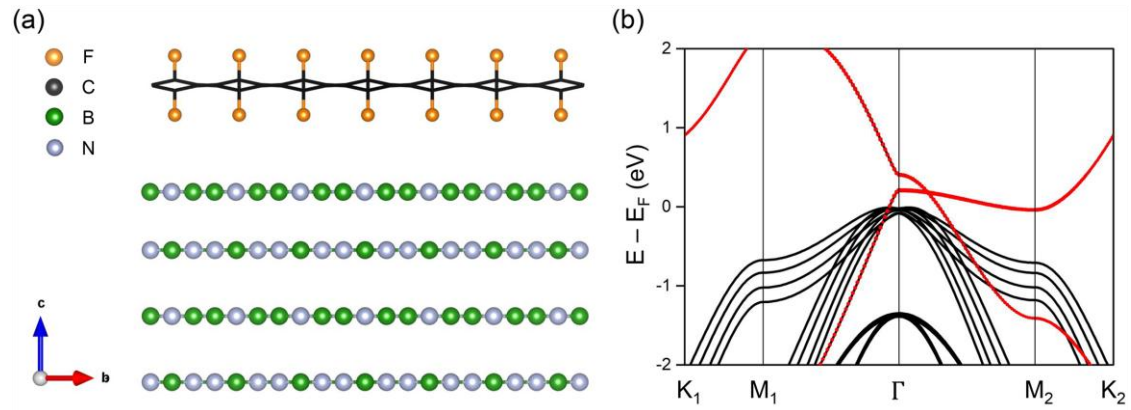
Fig. S13. 1×1 C_6F_2 on 1×1 BN (0001) substrate. (a) Side view of the layered structure. The lattice mismatch is 2%. (b) Corresponding band structure. Here, the contribution from p_z orbitals of carbon atoms are marked by red circles and the circle size represents orbital weights.

11
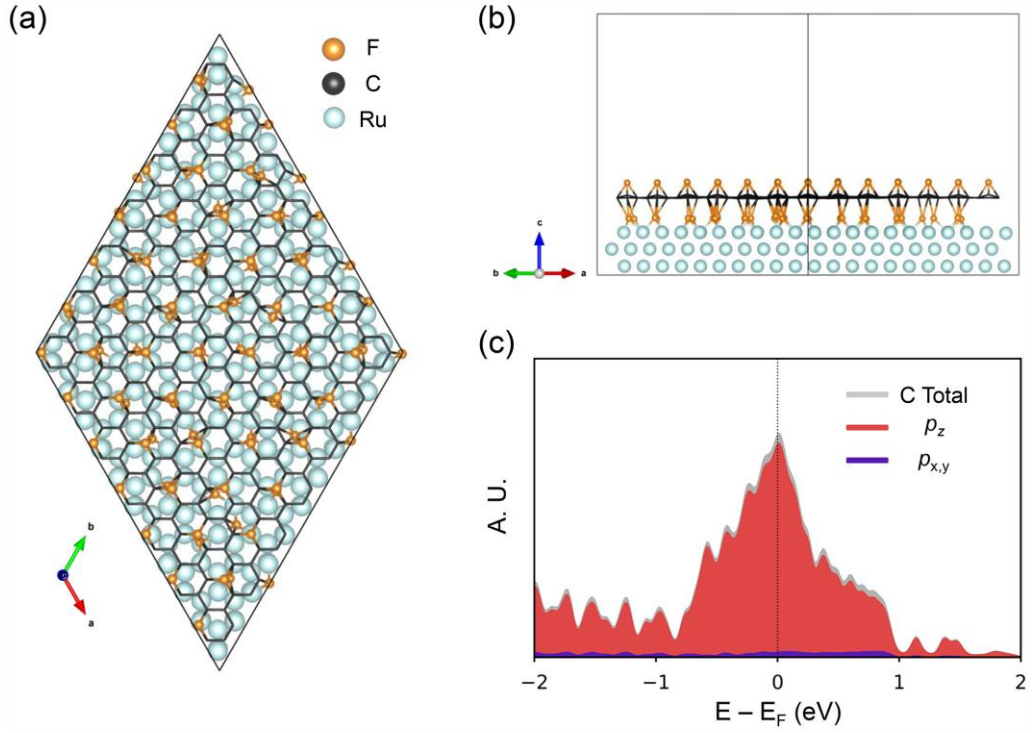
Fig. S14. 7×7 C_6F_2 on 11×11 Ru (0001) substrate. (a) Top view of the layered structure. (b) Side view. The lattice mismatch is 1.8%. (c) Projected DOS of the carbon atoms.

6. External Response of AC-Patterned Graphene

In Fig. S15, we show that the Dirac cones of AC-patterned graphene are movable along Γ-M_2 direction by uniaxial strain. In Fig. S16, the Kubo-Greenwood optical conductivity implies the anisotropic electrical response of AC-patterned graphene. In the low-frequency regions, σ_{xx} is much stronger than σ_{yy}. We discovered that the σ_{xx} absorption peak of type-II C_6F_2 is shifted to 1.53 eV, which is attributed to direct optical transition at M_2 point.
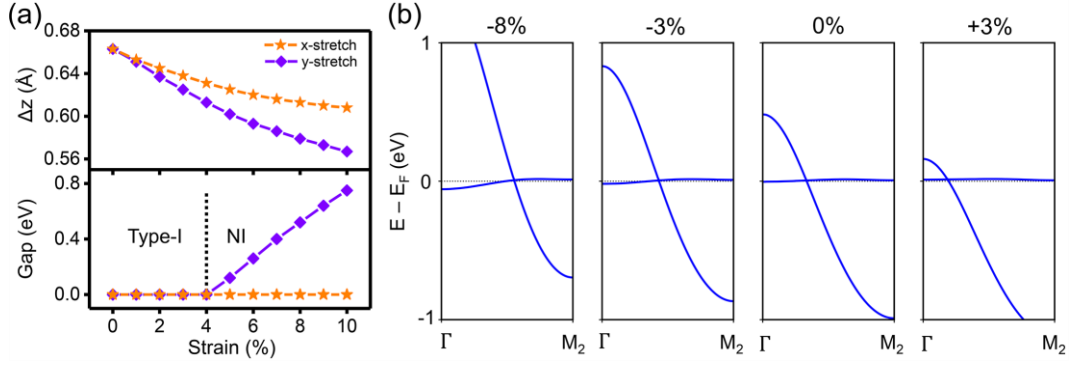
Fig. S15. (a) C_6H_2 energy gap and sp^3 carbon buckling Δz as a function of uniaxial tensile strain. The tilted type-I to NI phase transition happens at 4% y direction tensile strain. (b) C_6Cl_2 band structure evolution under y-direction strain. The type-III Dirac cones remain while the Dirac points shift as the strain varies.
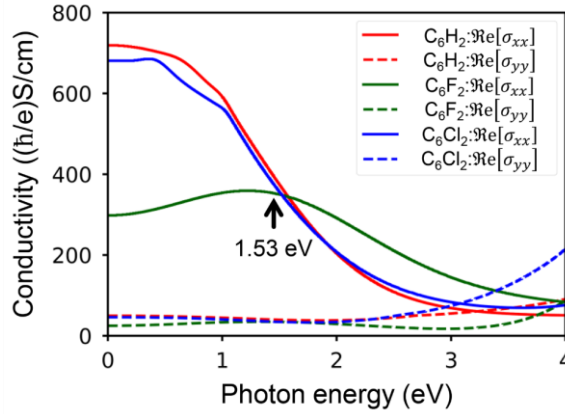
Fig. S16. Kubo-Greenwood optical conductivity tensors of C_6H_2, C_6F_2 and C_6Cl_2

7. Edge Bands of AC-Patterned Graphene

According to the symmetry and atomic distribution of AC-patterned graphene, we chose three types of edge directions Z1 (y,[$\bar{1}1$]), A1 (x, [11]), A2 ([10]) and four unit cell shapes for constructing nanoribbons in Fig. S17. Here, the symbols Z (A) follow the convention of zigzag (armchair) edges of pristine graphene nanoribbon. We considered the spinless case of C_6H_2, C_6F_2 and C_6Cl_2 and the spinful case of C_6Br_2.
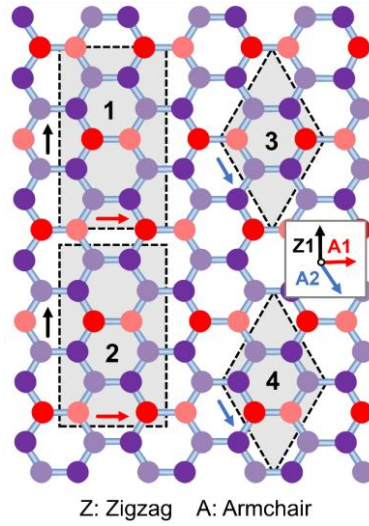
Fig. S17. Schematics of the selected unit cells 1, 2, 3, 4 for constructing nanoribbons. Here, purple (red) sites stand for sp^2 (sp^3) carbons. Conventional cell 2 breaks M_{xz} and the black, red, blue arrows denote periodic directions Z1, A1, A2, respectively.
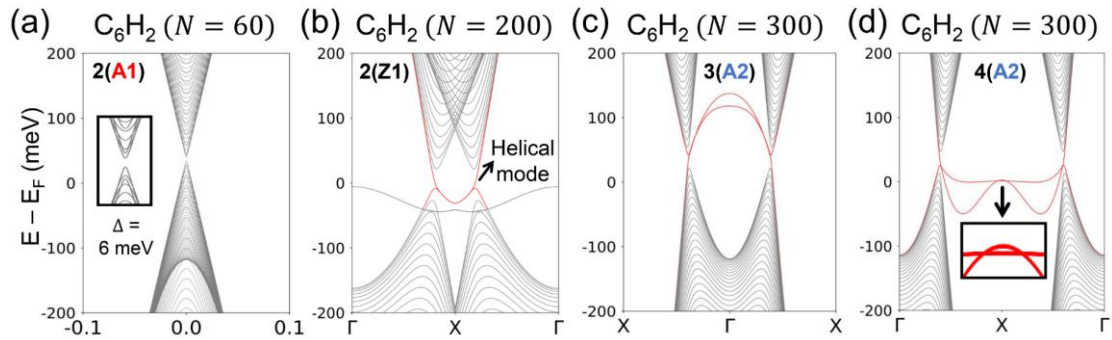
Fig. S18. MLWF calculated edge band structures of C_6H_2 nanoribbons. (a) The quantum confinement effect opens a small gap along A1 direction. (b) Two pairs of helical mode protected by C_{2y} symmetry and time-reversal symmetry appear along Z1 direction. (c,d) The C_{2y} mass term opens a gap between two Kramers pairs of C_6H_2 edge bands at a finite ribbon width.
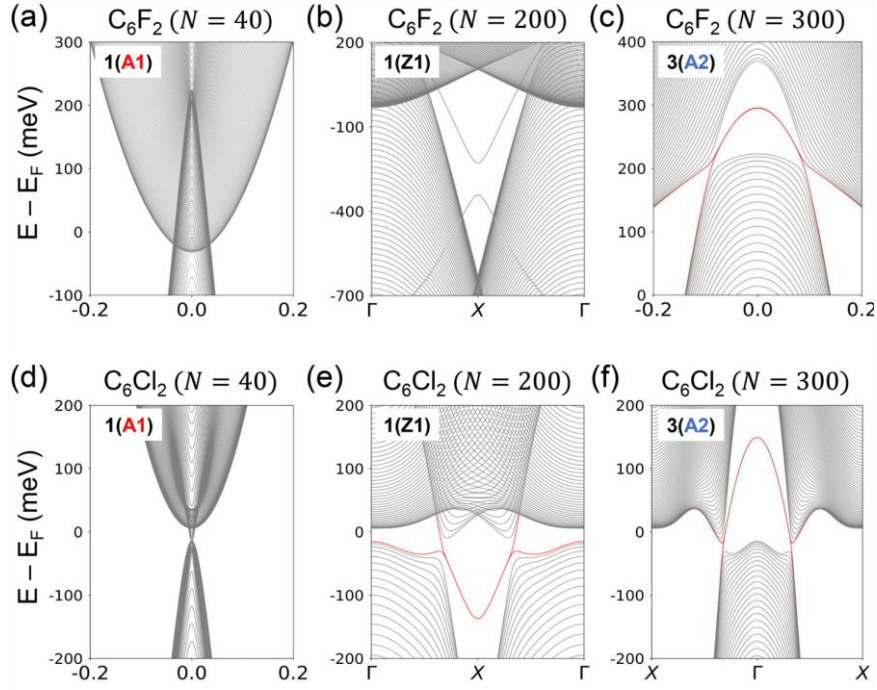
Fig. S19. MLWF calculated spinless edge band structures of C_6F_2 and C_6Cl_2 nanoribbons. (a-c) C_6F_2 periodic along A1, Z1, A2 directions and (d-f) C_6Cl_2 periodic along A1, Z1, A2 directions, respectively. In (b), two helical modes of type-II C_6F_2 have not yet intersected for the ribbon width $N = 200$. In (c) and (f), the C_{2y} mass term is too small to open a gap between the two Kramers pairs at Γ point.

8   Edge Spectra of AC-Patterned Graphene
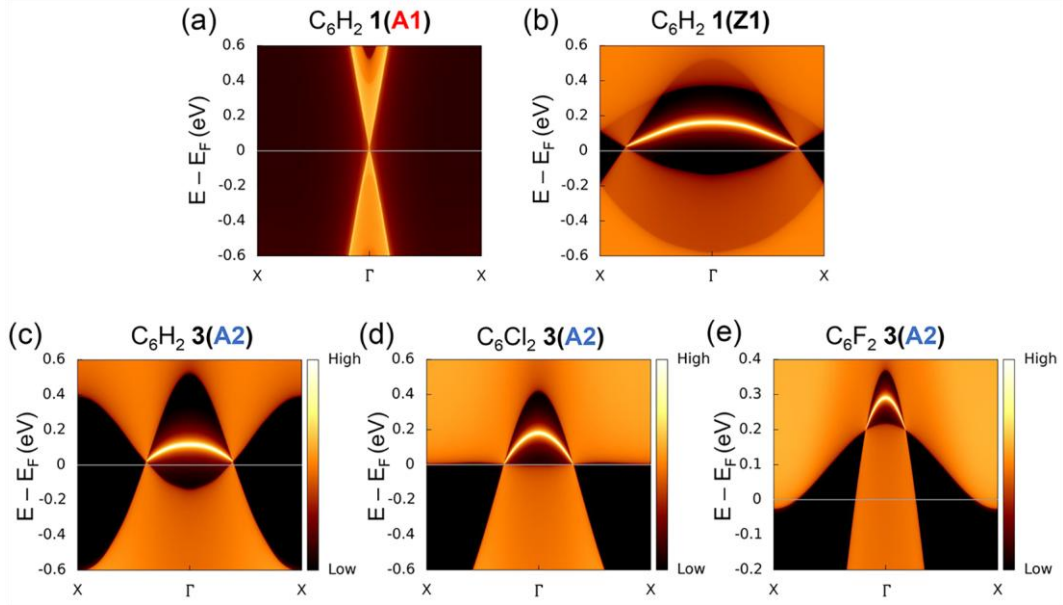
Fig. S20. Semi-infinite edge spectra of C_6X_2 (X = H, F, Cl). (a,b) Tilted type-I C_6H_2 periodic along A1 and Z1 directions. They resemble edge spectra of graphene in armchair and zigzag nanoribbon geometry, respectively. (c-e) C_6H_2, C_6Cl_2, C_6F_2 periodic along A2 direction, respectively. Compared with A1 direction, the two degenerate bulk Dirac cones shift away from Γ point due to C_{2y} breaking.
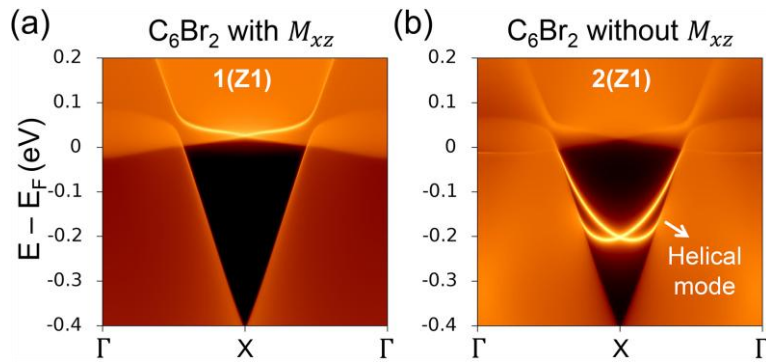
Fig. S21. Semi-infinite spectral functions of spinful C_6Br_2 periodic along Z1 direction. Comparing (a) and (b), the helical modes in C_6Br_2 with massive type-II Dirac fermions appear only if the mirror symmetry M_{xz} is broken.

16

9 Band Irreducible Representations

Lastly, we listed the symmetry information of the A-RA type CCM and AC-patterned honeycomb monolayers in Table S1 and S2, respectively.

Phase	TRIM	VB	CB	$\mathbb{Z}_2$ Invariant
Type-I Dirac cone	Γ	A_g A_u	B_g B_u	1
	M_1	A_u A_g	A_u A_g	
	M_2	A_u B_u	A_g B_g	
Type-II Dirac cone	Γ	A_g A_u	B_g B_u	1
	M_1	A_u A_g	A_u A_g	
	M_2	A_u B_u	A_g B_g	
Type-III Dirac cone	Γ	A_g A_u	B_g B_u	1
	M_1	A_u A_g	A_u A_g	
	M_2	A_u B_u	A_g B_g	
Gapped at Γ	Γ	A_g B_g	A_u B_u	0
	M_1	A_u A_g	A_u A_g	
	M_2	A_u B_u	A_g B_g	
Gapped at M_2	Γ	A_g A_u	B_g B_u	0
	M_1	A_u A_g	A_u A_g	
	M_2	A_u A_g	B_u B_g	

Table S1. A-RA type CCM band irreducible representations (irreps) for $t_2 < 0$ and $t_3 > 0$ without SOC. TRIM, VB and CB stand for time-reversal-invariant momenta, valence band and conduction band, respectively. According to Fu-Kane formula in the presence of inversion symmetry,[15] the time-reversal invariant $\mathbb{Z}_2 = \delta(\Gamma)\delta(M_1)^2\delta(M_2)$ and $\delta(K \in TRIM) = \prod_{n=1}^{VB} \xi_n(K)$, where ξ_n is the parity of the nth occupied band.

Formula	TRIM	VB	CB	SI
C_6H_2	Γ	$A_g B_u A_g A_u B_g A_u A_g B_u A_g B_u B_g A_g A_u$	$B_g A_g$	(0,0,1;0) for IC at (0,5,0.5,0.5) (0,0,1;2) for IC at (0,5,0.5,0.0)
	M_1	$A_g A_u A_g A_u A_u A_g A_u A_g A_g A_u A_g A_u A_g$	$A_g A_u$	
	M_2	$A_u A_g B_u A_g B_u B_g B_u A_u A_g A_g A_u B_g B_u$	$A_g A_u$	
C_6H_2 (+10% y stretch)	Γ	$A_g A_g A_u B_u B_g A_u A_g B_u A_g B_u B_g A_g B_g$		(0,0,0;0)
	M_1	$A_g A_u A_g A_u A_u A_g A_u A_g A_u A_g A_g A_u A_g$		
	M_2	$A_u A_g B_u A_g B_u B_g A_u B_u A_u A_g A_g B_g B_u$		
C_6F_2	Γ	$A_g B_u A_g A_g A_u B_u B_g A_u A_g B_u A_g B_g B_u A_g B_u A_u A_g B_g A_u$	$B_g A_g$	(0,0,1;0) for IC at (0,5,0.5,0.5) (0,0,1;2) for IC at (0,5,0.5,0.0)
	M_1	$A_g A_u A_u A_g A_g A_u A_u A_g A_g A_u A_g A_u A_g A_u A_g A_u A_g A_u A_g$	$A_u A_g$	
	M_2	$A_g B_u A_u A_g B_u A_g B_u B_g A_g B_u A_g A_u A_u A_g B_u B_u A_g B_g B_u$	$A_g B_u$	
C_6Cl_2	Γ	$A_g B_u A_g A_u B_g A_g B_u A_u A_g B_u A_g B_u B_g A_g B_u A_u A_g B_g A_u$	$B_g A_g$	(0,0,1;0) for IC at (0,5,0.5,0.5) (0,0,1;2) for IC at (0,5,0.5,0.0)
	M_1	$A_g A_u A_u A_g A_g A_u A_u A_g A_g A_u A_g A_u A_g A_g A_u A_u A_g A_u A_g$	$A_u A_g$	
	M_2	$A_g A_u B_u A_g B_u A_g B_u B_g A_u B_u A_g A_u A_g B_g A_u B_u A_g B_g B_u$	$A_g B_u$	
C_6Br_2	Γ	$A_g B_u A_g A_u B_g A_g B_u A_u A_g B_u A_g B_g B_u A_g A_u B_u A_g B_g A_u$	$B_g A_g$	(0,0,1;0) for IC at (0,5,0.5,0.5) (0,0,1;2) for IC at (0,5,0.5,0.0)
	M_1	$A_g A_u A_g A_u A_g A_u A_u A_g A_g A_u A_g A_u A_g A_u A_g A_u A_g A_u A_g$	$A_u A_g$	
	M_2	$A_g A_u B_u A_g B_u A_g B_u B_g A_u A_g B_u A_u B_g A_g A_u B_u B_g A_g B_u$	$A_g B_u$	
Si_6H_2	Γ	$A_g A_g B_u A_u B_g B_u A_u A_g A_g B_u A_g B_g A_u$		(0,0,1;0) for IC at (0,5,0.5,0.5) (0,0,1;2) for IC at (0,5,0.5,0.0)
	M_1	$A_g A_u A_g A_u A_u A_g A_u A_g A_u A_g A_g A_g A_u$		
	M_2	$A_g A_u B_u A_g B_u B_g A_g B_u A_u A_g A_u B_g B_u$		

Table S2. First-principles calculated band irreps and symmetry-based indicators (SIs)[16,17] by treating $C2/m$ layer group as No. 12 space group. The band irreps listed here are spinless results. The double space group irreps with SOC are extracted to calculate the $\mathbb{Z}_{2,2,2,4}$ SIs (0,0,1;0) and (0,0,1;2) SIs are equivalent but convention-dependent,[17] they indicate 2D TI or spinless semimetal phases with $\mathbb{Z}_2 = 1$ or topological crystalline insulator states by stacking 2D TIs. The difference between them is the chosen inversion center (IC) during the slab calculation.

18

REFERENCES

[1] Kresse G, Furthmuller J 1996 *Phys. Rev. B* **54** 11169

[2] Perdew J P, Burke K, Ernzerhof M 1996 *Phys. Rev. Lett.* **77** 3865

[3] Giannozzi P, Baroni S, Bonini N, Calandra M, Car R, Cavazzoni C, Ceresoli D, Chiarotti G L, Cococcioni M, Dabo I, Dal Corso A, de Gironcoli S, Fabris S, Fratesi G, Gebauer R, Gerstmann U, Gougoussis C, Kokalj A, Lazzeri M, Martin-Samos L, Marzari N, Mauri F, Mazzarello R, Paolini S, Pasquarello A, Paulatto L, Sbraccia C, Scandolo S, Sclauzero G, Seitsonen A P, Smogunov A, Umari P, Wentzcovitch R M 2009 *J. Phys. Condens. Matter* **21** 395502

[4] Marzari N, Vanderbilt D 1997 *Phys. Rev. B* **56** 12847

[5] Mostofi A A, Yates J R, Pizzi G, Lee Y S, Souza I, Vanderbilt D, Marzari N 2014 *Comput. Phys. Commun.* **185** 2309

[6] Sancho M P L, Sancho J M L, Rubio J 1985 *J. Phys. F* **15** 851

[7] Wu Q S, Zhang S N, Song H F, Troyer M, Soluyanov A A 2018 *Comput. Phys. Commun.* **224** 405

[8] Garc á J H, Covaci L, Rappoport T G 2015 *Phys. Rev. Lett.* **114** 116602

[9] Liu F, Deng H Y, Wakabayashi K 2019 *Phys. Rev. Lett.* **122** 086804

[10]Kane C L, Mele E J 2005 *Phys. Rev. Lett.* **95** 146802

[11]Liu C C, Jiang H, Yao Y G 2011 *Phys. Rev. B* **84** 195430

[12]Liu C C, Guan S, Song Z G, Yang S Y A, Yang J B, Yao Y G 2014 *Phys. Rev. B* **90** 085431

[13]Lu H-Y, Cuamba A S, Lin S-Y, Hao L, Wang R, Li H, Zhao Y, Ting C 2016 *Phys. Rev. B* **94** 195423

[14]Grimme S 2006 *J Comput. Chem.* **27** 1787

[15]Fu L, Kane C L 2007 *Phys. Rev. B* **76** 045302

[16]Khalaf E, Po H C, Vishwanath A, Watanabe H 2018 *Phys. Rev. X* **8** 031070

[17]Song Z, Zhang T, Fang Z, Fang C 2018 *Nat. Commun.* **9** 3530